

**Properties of the Hermean regolith: IV. Photometric
parameters of Mercury and the Moon contrasted with Hapke
modelling**

J. Warell

Institutionen för Astronomi och Rymdfysik, Uppsala Universitet, Box 515, SE-751 20

Uppsala, Sweden

E-mail: johan.warell@astro.uu.se, Telephone: +46 18 471 5970, Fax: +46 18 471 5999

Proposed running head: Regolith Properties of Mercury IV

Address editorial correspondence and proofs to:

J. Warell

Institutionen för Astronomi och Rymdfysik

Uppsala Universitet

Box 515

SE-751 20 Uppsala

Sweden

Received _____; accepted _____

Abstract

A comparison of the photometric properties of Mercury and the Moon is performed, based on their integral phase curves and disk-resolved image data of Mercury obtained with the Swedish Vacuum Solar Telescope. Proper absolute calibration of integral V-band magnitude observations reveals that the near-side of the Moon is 10–15% brighter than average Mercury, and 0–5% brighter for the "bolometric" wavelength range 400–1000 nm. As shown, this is supported by recent estimates of their geometric albedos. Hapke photometric parameters of their surfaces are derived from identical approaches, allowing a contrasting study between their surface properties to be performed. Compared to the average near-side Moon, Mercury has a slightly lower single-scattering albedo, an opposition surge with similar or smaller width (indicating similar top-soil porosity) and of marginally smaller amplitude, and a somewhat smoother surface. The width of the lobes of the single-particle scattering function are smaller for Mercury, and the backward scattering anisotropy is stronger. In terms of the double Henyey-Greenstein b - c parameter plot, the scattering properties of an average particle on Mercury is closer to the properties of lunar maria than highlands, indicating a higher density of internal scatterers than that of lunar particles. The photometric roughness of Mercury is well constrained by the recent study of Mallama *et al.* (2002, *Icarus* 155, 253) to a value of about 8° , suggesting that the surfaces sampled by the highest phase angle observations (Borealis, Susei and Sobkou Planitia) are lunar mare-like in their textural properties. However, Mariner 10 disk brightness profiles obtained at intermediate phase angles indicate a surface roughness of about twice this value. The photometric parameters of the Moon are more difficult to constrain due to limited phase angle coverage, but the best Hapke fits are provided by rather small surface roughnesses. Better-calibrated, multiple-wavelength

observations of the integral and disk-resolved brightnesses of both bodies, and obtained at higher phase angle values in the case of the Moon, are urgently needed to arrive at a more consistent picture of the contrasting light scattering properties of their surfaces.

Subject headings: Mercury; Moon; Regoliths; Surfaces, Planets;

1. Introduction

The photometric properties of Mercury and the Moon have been studied by many authors based on different data sets (Danjon 1949, Dollfus and Auriere 1974, Mallama *et al.* 2002 for Mercury; Russell 1916, Rougier 1933, Nikonova 1949, Shorthill 1969, Lane and Irvine 1973 for the Moon) and different photometric theories such as Hapke’s (1981, 1984, 1986, 1993, 2002), Lumme and Bowell’s (1981a) and Shkuratov *et al.*’s (1999b). For Mercury, photometric quantities have been derived from the integral phase curve (Danjon 1949, de Vaucoeleurs 1964, Lumme and Bowell 1981a, Veverka *et al.* 1988, Bowell *et al.* 1989, Domingue *et al.* 1997, Hartman and Domingue 1998, Mallama *et al.* 2002) and Mariner 10 images (Hapke 1984, Bowell *et al.* 1989, Robinson and Lucey 1997). Quantities for the Moon have been determined from a wider variety of data sets combining or treating separately observations of the integral disk and the resolved surface (e.g., Harris 1961, Lane and Irvine 1973, Lumme and Bowell 1981b, Lumme and Irvine 1982, Shevchenko 1982, Helfenstein and Veverka 1987, Helfenstein *et al.* 1997, Hartman and Domingue 1998, Hillier *et al.* 1999, Shkuratov *et al.* 1999a, Kreslavsky *et al.* 2000).

The photometric properties of the two bodies, derived from Hapke’s (1986) theory, were contrasted by Veverka *et al.* (1988). They modelled both bodies with the same approach from Danjon’s (1949) integral phase curve for Mercury, and from the integral phase curve observations of Shorthill *et al.* (1969) and Lane and Irvine (1973) for the Moon. This kind of parallel modelling is important for providing a solid basis of interpretation for such photometrically similar bodies.

The main conclusion of Veverka *et al.* (1988) was that the photometric parameters of Mercury and the Moon are very similar. Specifically, their photometric roughnesses and particle single-scattering albedos were determined to be nearly identical, but with the opposition surge somewhat stronger and wider, and the backscattering asymmetry slightly more pronounced for the Moon. Except for the relative backscattering asymmetry their results are similar to those obtained here. However, their results are prone to error since

the phase angle range was limited to 3–123° for Mercury, and 2–145° for the Moon. Thus the observations did not sample well either their opposition surges (critical to deriving the absolute magnitude and geometric albedo) or their crescent phases (critical to determining the surface roughness). These problems are discussed by Domingue and Hapke (1989).

In this work, a new critical comparison of the photometric properties of the Moon and Mercury is performed, using exactly the same approach for both bodies, and incorporating several improvements relative to the work of Veverka *et al.* (1988). The better developed model formulation of Hapke (1993, 2002), a more appropriate double Henyey-Greenstein representation of the particle angular scattering function (Veverka *et al.* 1988 employed a three-term Legendre particle phase function), the more complete phase curve observations of Mallama *et al.* (2002) for Mercury, and high-resolution disk-resolved ground-based imaging observations from Warell and Limaye (2001) are used to better constrain the parameter values. As such, this is the first study to combine phase curve and resolved disk observations in the derivation of Hapke photometric parameters for Mercury. Also considered are the effects of probable calibration errors of earlier observations and of their limited phase angle range, the latter of which is specifically crucial to the determination of the surface roughness.

The disk-integrated V-band observations of Mallama *et al.* (2002, covering phase angles 2–170°) has considerably improved the phase coverage for the case of Mercury. For the Moon, the best data set is still that of Lane and Irvine (1973), for which the highest observed phase angle is 145°. The coverage for Mercury is complete enough to determine a value for the surface roughness with a small error range, though the opposition surge cannot be determined with much confidence. The situation is reversed for the Moon, where data for high phase angles are lacking, thus limiting the possibility of determining the surface roughness from the integral phase curve, but its opposition effect has been well studied from orbiter data (Helfenstein *et al.* 1997, Hillier *et al.* 1999, Shkuratov *et al.* 1999a).

Since the coherent backscatter contribution to the opposition surge (Hapke 2002 and references therein) for Mercury can not presently be modelled due to limited phase angle coverage, coherent backscattering is not treated separately here. Intensity contributions other than shadow hiding to the amplitude of the opposition surge are allowed by letting B_0 exceed unity (e.g., Hapke 1981, Helfenstein *et al.* 1997), which will adequately account for the the total opposition effect. This simplified but robust approach is used for both the Moon and Mercury.

The question of the relative albedo of Mercury and the Moon is also studied. Throughout the literature, the geometric albedos of the two bodies are used as a robust measure of their absolute reflectances. The use of the geometric albedo for such comparative purposes is highly questionable since it depends critically on the total amplitude of the opposition surge. In the case of the Moon, the opposition intensity increases by about 40% from 4° to 0° phase angle (Buratti *et al.* 1996), and by about 10% for phase angles $< 1^\circ$ (Shkuratov *et al.* 1999a). The effect may be similar for Mercury, but with present phase angle observations restricted to $> 2.2^\circ$ the possibility to confidently quantify it is limited. A comparison of the brightnesses of Mercury and the average near-side Moon is performed without resorting to determinations of their geometric albedos.

2. Hapke’s photometric model

The bidirectional reflectance function in Hapke’s (1993) photometric theory is described with several parameters: the particle single-scattering albedo w , the opposition effect width h , the opposition effect amplitude B_0 , the subresolution-scale mean surface roughness angle $\bar{\theta}$, and two or three parameters describing the shape of the angular particle scattering function of the average particle $p(\alpha)$ (single-particle phase function). In this work, use has been made of Hapke’s (2002) improved second-order approximation for the Ambartsumian-Chandrasekhar H -functions in the expression for the bidirectional reflectance, and of the improved model for the anisotropic component of multiple scattering

(the M term in the expression for the bidirectional reflectance). Both these recent improvements should produce more reliable parameter values, though results for the bidirectional reflectance and the particle phase function parameters may not be directly comparable to that of the previous work mentioned above.

For the particle angular scattering function, the double Henyey-Greenstein (2-HG) description was adopted as it provides a good representation of the double-lobed scattering properties of real particles while at the same time restricting the number of model parameters. Hartman and Domingue (1998) studied the importance of the choice of the representation of the single-particle angular scattering function based on the experimental particle measurements of McGuire and Hapke (1995). They found that either of the two-parameter (double lobe) phase curve representations based on the three first Legendre polynomials or a linear combination of two Henyey-Greenstein functions is preferable to their single lobe expressions if the phase coverage extends above 30° in phase angle; that the 2-HG function is a better choice than the linear combination of the three first Legendre polynomials in practically all cases; that a 2-HG function offers the most ideal choice in terms of minimizing the number of model parameters and possibility to fit the phase curve data within current observational error for a phase angle coverage of $< 130^\circ$; and that the added complexity of a three-term Henyey-Greenstein function does only motivate its use for very high-quality data or very extended phase curve coverage. Hartman and Domingue (1998) also showed that observations at phase angles above about 120° are necessary to constrain the relative amplitudes of the forward and backward scattered lobes of the particle angular scattering function, and that determination of other model parameters could be highly influenced by the choice of phase function representation. From their experimental work, McGuire and Hapke (1995) demonstrated that the use of a 2-HG representation is preferable to a double Legendre polynomial when the scattering function has a narrow forward lobe. In one of the model applications described below (method *III*), disk-resolved data unconstrained by the integral phase curve are fit for a limited intermediate phase angle range and the 2-HG representation is then clearly superior. Its

consequent use in all modelling thus makes the results inter-comparable. Additionally, this representation of the scattering function conforms to the HG parameter plot for single-particles experimentally measured by McGuire and Hapke (1995), and thus allows an interpretation of the results in terms of the properties of real particles.

There are several possible representations of the 2-HG function. The form used here, due to McGuire and Hapke (1995), is

$$p_{\text{HG}}(\alpha) = \frac{1+c}{2} \frac{1-b^2}{(1-2b \cos \alpha + b^2)^{3/2}} + \frac{1-c}{2} \frac{1-b^2}{(1+2b \cos \alpha + b^2)^{3/2}},$$

where $b \in [0, 1]$ describes the angular width of the forward and backward scattering lobes (isotropically scattering particles have $b = 0$), and c (unconstrained, but $p_{\text{HG}} \geq 0 \forall \alpha$) the amplitude of the backscattered lobe relative to the forward scattered lobe (for backscattering particles, $c > 0$). In this two parameter form, the scattering lobes are assumed to be equally wide.

It has been demonstrated (Domingue and Hapke 1989, Helfenstein and Veverka 1989) that determination of unique parameter values is not possible from integral phase curve data alone without resorting to pre-determined constraints and full phase curve coverage, but that unique values may be obtained from disk-resolved observations. These effects are considered in the extensive photometric modelling of lunar disk-resolved and integral phase curve observations by Helfenstein *et al.* (1997), and for Clementine disk-resolved photometry by Hillier *et al.* (1999). In the case of the mercurian phase curve, we are now in a better position to determine the relative contributions of forward and backward scattering than for the average remotely sensed Moon, for which current integral phase curve data exists for a more limited range of 1.4–144.5° (cf. Helfenstein *et al.* 1997). It is shown below however, that even though using the best-choice representation for the particle angular scattering function the currently available data for the mercurian phase curve remains insufficient to constrain the Hapke parameters uniquely, even in combination with the best ground-based disk-resolved images, due to the large photometric scatter in the data. The situation is even worse when considering the wavelength dependence

of the Hapke parameters; though spectroscopic observations have been performed since the 1960's, photometrically usable multiple-wavelength information is available only from SVST image data and this data set is only in part complemented with absolute flux calibration observations (Warell 2002).

3. Hapke modelling

As Hapke's bidirectional reflectance function is based on many parameters, each of which influences the calculated reflectance of resolved planetary disk profiles and integral phase curves in part similarly, it has multiple solutions which are more or less reasonable (Domingue and Hapke 1989, Helfenstein and Veverka 1989). The problem of parameter determination was approached from a totally unbiased viewpoint by fitting the function via a grid-search method, rather than using "smart" RMS-minimizing methods to find good solutions in parameter space, or relying on parameter sets determined or guessed as likely by other authors. With the present approach, good solutions to the Hapke function which are different from those found previously are less likely not to be detected, and the deepest global minimum in parameter space is more likely to be identified rather than one of several local RMS minima.

The modelling was performed with three methods incorporating different combinations of data sets. In method *I*, the V-filter integral phase curve data of Mallama *et al.* (2002) was fitted. The goodness-of-fit was determined in magnitude representation in a least-squares sense with the RMS residual measure

$$\text{RMS}_1 = \left[\frac{2.5^2}{N} \sum_i^N (\log_{10} R_i - \log_{10} I_i)^2 \right]^{1/2}, \quad (1)$$

where R_i are the modelled radiance factors (πr , where r is the bidirectional reflectance) of the integrated disk at phase angle α_i , I_i the corresponding observed brightnesses, and N

the number of data points.

In method *II*, intensity profiles from the luminance equator and central meridian (zero luminance longitude) of SVST images were modelled simultaneously with the phase curve of Mallama *et al.* (2002), and this method should therefore be able to better constrain the parameters. V-band or 550 nm images were employed. Additionally, 650 nm image data, scaled in brightness to the 550 nm reflectance of Mercury, were used to expand the data base. The brightness scaling was based on the calculated geometric albedos at the two wavelengths from Warell (2002), Table I. In terms of other sources of error the assumption of constant phase function of the surface from 550 to 650 nm makes a negligible contribution to the total error.

The goodness-of-fit in the second method was determined in a least-squares sense from the RMS residual measure

$$\text{RMS}_2 = \frac{1}{2} \left[\frac{2.5^2}{M_i + M_j} \left(\sum_i^{M_i} (\log_{10} R_i - \log_{10} I_i) + \sum_j^{M_j} (\log_{10} R_j - \log_{10} I_j) \right)^2 w_{ij} \right]^{1/2} + \frac{1}{2} \text{RMS}_1. \quad (2)$$

Here, i 's and j 's refer to points on the equatorial and central meridian profiles, respectively, and $w_{ij} = R_{ij} / \max \{ [R_{11}, R_{21}, \dots, R_{i,1}] [R_{11}, R_{12}, \dots, R_{1,j}] \}$ are weighting factors assigned on each profile data point to put less weight on low reflectance values in response to their lower signal-to-noise ratios and the stronger relative importance of scattered light.

With method *III* it was investigated whether parameter values were obtainable, from disk-resolved image data only, for other wavelengths than 550 nm, with the best-fit parameter values determined in intensity form by minimizing

$$\text{RMS}_3 = \left[\frac{1}{M_i + M_j} \left(\sum_i^{M_i} (R_i - I_i) + \sum_j^{M_j} (R_j - I_j) \right)^2 w_{ij} \right]^{1/2}. \quad (3)$$

Here, R_{ij} are the modelled radiance factors of the i, j :th points of the disk profiles, I_{ij} the corresponding observed brightnesses, $M_{i,j}$ the number of profile data points, and $w_{i,j}$ their respective weights as in Eq. 2.

As to the range of the model parameters allowed in the fitting procedure, w , b and h were constrained to their theoretical limits (e.g., Hapke 1993), the range for c was somewhat extended compared to the range found for naturally occurring single particles (McGuire and Hapke 1995), and values for $\bar{\theta}$ extend beyond the range determined for atmosphere-less solar system bodies (e.g., Helfenstein and Veverka 1987). The value of B_0 has been allowed to fall well outside its theoretical range ($0 - 1$) to account for the effect of a coherent backscattering contribution to the shadow hiding opposition surge (e.g., Helfenstein *et al.* 1997). In all three methods, initial searches for the best-fit Hapke solution employed the widest possible parameter grid ($0 < w < 1$, $0 < b < 1$, $-2 < c < 2.5$, $0 < h < 1$, $0 < B_0 < 5$, and $0 < \bar{\theta} < 50^\circ$). Several subsequent iterative runs with narrower parameter ranges centered on the previously determined best-fit distributions were then performed until the parameter values stabilized.

In methods *I* and *II* the absolute magnitude of Mercury was constrained to -0.45, and that of the Moon to +0.15, at a phase angle of 3° as given by integral phase curve observations. In a separate solution, the phase angle range for Mercury was additionally constrained to match that of the Rougier (1933) integral phase curve observations of the Moon to study the effects of limited phase angle coverage and the implications for the comparison of mercurian and lunar photometric parameters (Sec. 6.2).

4. Integral phase curve data for Mercury and the Moon

The phase curve observations of Mallama *et al.* (2002) offer the first possibility to roughly estimate the opposition effect parameters h and B_0 for Mercury, as well as to determine the relative contributions of the forward and backward lobes in the particle

scattering function. The previously most complete phase curve coverage is that of Danjon (1949) who measured Mercury’s brightness for the range $3\text{--}123^\circ$. Danjon’s data have been analyzed with Hapke’s theory by a number of authors (Veverka *et al.* 1988, Bowell *et al.* 1989, Domingue *et al.* 1997) and various parameter sets have been presented that fit the observations reasonably well.

For the Moon, the photoelectric observations of Rougier (1933) for a wavelength of 445 nm were used. This data set was converted to absolute V-band magnitude by multiplying each data point with the same factor, determined from the brightnesses of the 548 nm photoelectric observations of Lane and Irvine (1973). The data set of Rougier was used rather than that of Lane and Irvine due to the larger phase angle coverage of the former ($2.4^\circ < \alpha < 144.5^\circ$ compared to $6.6^\circ < \alpha < 118.6^\circ$). In performing the scaling, the assumption is made that the phase function is wavelength independent (similar to Helfenstein and Veverka 1987, Helfenstein *et al.* 1997). The adequacy of this assumption is discussed in Sec. 7.1.

5. Disk-resolved image data of Mercury

The disk-resolved data set employed here was selected from that presented in Warell and Limaye (2001) and consists of the highest resolution images obtained with the SVST at five apparitions of Mercury in 1995 through 1999. At least two images per apparition in the wavelength range 550–940 nm were used, though for 1996 and 1999 the data was restricted to one wavelength (750 and 650 nm, respectively). The phase angle range is $63^\circ\text{--}89^\circ$. The sharpest images are of diffraction-limited resolution, though the near-infrared images have lower resolution due to telescope-inherent chromaticity. All images were subjected to dark-subtraction, flat-fielding and sky subtraction. Information specific to the images used here are given in Table 3 (cf. also Table 4 of Warell and Limaye 2001).

5.1. Modelling the seeing smear

Though of high angular resolution, the SVST image data set suffers from degradation of the resolution due to seeing, chromatic aberration and the optical diffraction limit. The 0.5-m aperture of the SVST provides a theoretical diffraction limit of about $0.23''$ at 550 nm, a value which was reached for the sharpest 550 and 650 nm images (Table 3). The effect of limited resolution on the observed brightness distribution of Mercury’s disk is illustrated in Fig. 1 for a profile along the luminance equator at an intermediate phase angle. The point of maximum intensity is shifted increasingly towards the disk center at deteriorating seeing and the highly discriminative intensity surge at the limb is lost by limiting the resolution. The general shape of the disk profile at the terminator remains however well preserved for an effective seeing smear of about $\sigma < 0.4''$.

To allow a comparison of modelled and observed disk intensity profiles, calculated equatorial and central meridian profiles of the image data were convolved with a flux conserving gaussian to simulate seeing smear. The width of the smearing gaussian was determined from Hapke reflectance models for the observed geometries using the parameters determined by Robinson and Lucey (1997) based on disk-resolved Mariner 10 image data, computed here for a cylindrical grid with 1-degree resolution in both axes. These reflectance maps were projected to spherical geometry, rebinned to the proper pixel scale, and convolved with a range of two-dimensional, rotationally symmetric and flux-conserving gaussians of varying full-width half-maximum (FWHM) dimensions. The seeing-smear resolution of each image was found from a comparison of the brightness distribution of the observed disk images with that of convolved Mercury disk models. The accuracy with which the PSF width may be determined for an individual image is estimated to $< 0.03''$. The seeing estimates, presented in Table 3, were subsequently employed in the determination of optimal Hapke parameters from disk profile modelling.

5.2. Flux calibration

The flux calibration performed for Mariner 10 full-disk images and the relative disk-integrated spectrum of Warell (2002) were used to obtain the absolute reflectance (in radiance factors) of each image. The reflectance values of Mariner 10 disk profiles observed at phase angles of 77 and 106° (Hapke *et al.* 1975a, Hapke 1984) were compared with predictions from Hapke theory for the five phase angles observed with the SVST. The disk brightness distributions were modelled with the parameter sets of Robinson and Lucey (1997) and "solution 2" of Veverka *et al.* (1988). The predicted brightnesses were found to be slightly too faint relative to Mariner 10. It is known that the Mariner 10 flux calibration may be slightly in error (Hapke *et al.* 1975a, Mallama *et al.* 2002). Nevertheless, it was assumed that this calibration is correct, and the modelled phase curve for the maximum disk brightness was adjusted by +6%, which provided a good match.

The modelled luminance equator profiles for each image geometry were convolved with one-dimensional gaussians of proper widths to provide the observed maximum disk reflectance values at a wavelength of 550 nm. While the Danjon (1949) phase curve used by Veverka *et al.* (1988) is recalibrated for the V-band (554 nm), the effective wavelength of the Mariner 10 flux calibration is 575 nm (orange filter; Bowell *et al.* 1989). This small difference does not influence the absolute brightness; it is certainly within the observational error. To convert the modelled reflectance values to those at other wavelengths, the reflectances were scaled according to the relative geometric albedos of the integrated disk presented in Warell (2002), prior to solving the reflectance function for the SVST image data.

From each calibrated image, two disk profiles were then extracted by averaging the intensity of three pixel wide ($< 0.3''$) sections along the luminance equator and meridian. The use of two-dimensional data slices from perpendicular disk directions is preferable to using only single profiles since a larger range of luminance coordinates is sampled, which is beneficial in constraining the model parameters (e.g., the effect of varying $\bar{\theta}$ is most

prominent in meridional profiles). Full two-dimensional modelling of the complete set of disk pixels would require nearly two orders of magnitude longer computing time, and was not a realistic undertaking.

The error in the absolute Mariner 10 flux calibration is only one of several factors contributing roughly equally to the total error budget. Other sources of error are uncertainties in the estimation of the seeing, the assumption of a constant seeing smear across the disk, the contribution of scattered light (particularly important at the bright planetary limb), wavelength-dependent chromatic aberration and atmospheric refraction, isolated bright or dark albedo features which may deviate 10-20% in brightness relative to a uniform disk, and uncertainty of the dependence of geometric albedo with wavelength (the spectral slope for Mercury’s disk varies strongly with photometric geometry; Warell 2002, 2003). Basic data calibration issues (e.g., flat fields, dark frames, data linearity) and the signal-to-noise ratio are of minor concern in this respect. It may therefore be expected that the brightness across the disk may vary by as much as 20% from image to image. This influences the accuracy with which the model parameters may be determined and causes a range in their best-fit values.

6. Modelling results

6.1. Mercury

The solutions derived with methods *I* and *II* (Sol. 1–Sol. 3, Sol. 7) are given in Table 1 and 2 respectively and are compared with the Mallama *et al.* (2002) phase curve observations in Fig. 2. As expected, many parameter sets provide good fits to the data. However, the best fit for the restricted phase angle range $< 145^\circ$ (Sol. 3), which has a twice as large roughness as the other models, is too faint for high phase angles, though the RMS value is smaller than for Sol. 1 and Sol. 2. The average parameter set (Sol. 7) obtained with method *II* may be used to identify the most probable solution derived from

method *I*. The values of c and B_0 may be traded off against each other to lower the phase curve intensity at intermediate phase angles, which is necessitated with a low value of $\bar{\theta}$. The dependence of the integral brightness on B_0 is less than for c , which may therefore be constrained better. Based on Sol. 7 it is determined that Sol. 1, with a higher value for B_0 and a smaller w , is superior.

Other solutions to the integral phase curve with small RMS values may be excluded due to unphysical values of one or several parameters. E.g., increasing B_0 implies a low c but provides too small values for w . A small B_0 requires a large b and $\bar{\theta}$ and a moderate value of c , but makes fitting low phase angle observations impossible as the predicted phase curve will be generally too flat, too dark at high phase angles, and combine a faint opposition magnitude with a large w . Most importantly, the high intensity of large phase angle ($165^\circ < \alpha < 170^\circ$) observations require surface roughnesses of the order of 10° to be properly fit, irrespective of the choice of other parameters. This fact greatly limits the possible ranges of other parameters.

The larger RMS values of method *II* compared to method *I* solutions are attributable to albedo features on the mercurian disk, as illustrated in Fig. 7. An image with a bright albedo feature near the equatorial terminator (low i , high e) requires a more forward scattering single-particle phase function (low c) or a smoother surface (low $\bar{\theta}$) to fit the intensity profile adequately.

A good parameter fit based on disk-resolved data only (method *III*) was possible to find only by locking all parameters except for w and $\bar{\theta}$ to the values determined with method *II*. This resulted in an expected increase in particle single-scattering albedo with wavelength and a constant mean surface roughness angle (Table 3). The average value of $\bar{\theta}$ determined this way is slightly greater than that determined with the two other methods, but has a larger error. It is not possible with the current data set to investigate the wavelength dependence of b , c and B_0 , which may be expected to be present due to their dependence on the particle single-scattering albedo (Domingue and Hapke 1989). This

requires calibrated multicolor photometric data of the integral disk brightness.

6.2. The Moon

The resulting best-fit models for the Moon are given in Table 1 as Sol. 4 to Sol. 6, and are illustrated in Fig. 3. The best-fit is provided by Sol. 4 which has the smoothest surface, $\bar{\theta} = 11^\circ$. Compared to the other models, it predicts a moderate opposition magnitude and physical albedo combined with the best correspondence to the observations at both high and low phase angles. Generally, increasing $\bar{\theta}$ for this data set forces a high w , at the expense of a poorer fit to the observations at the lowest and highest phase angles. A large surface roughness of about 25° and higher is very difficult to fit properly to these data. The integral phase curve data thus indicates that the high surface roughness (27°) for the average Moon derived by Helfenstein *et al.* (1997) is not probable, particularly as it must be combined with a high single-particle scattering albedo ($w = 0.28$) to fit the observed opposition magnitude. Furthermore, if the Rougier (1933) data is corrected for the phase reddening effect, the derived value for $\bar{\theta}$ decreases further (see Sec. 7.1). From the lesson learned in restricting the mercurian phase angle range (Sol. 3 vs. Sol. 2), it is possible that an error in the derived surface roughness for the Moon may remain undetected due to the limited range of phase angle data. This further strengthens the case for a small lunar surface roughness.

As in the present study, Helfenstein and Veverka (1987) modelled the integral phase curve considering shadow-hiding only and with B_0 unconstrained, but used a three-term Legendre polynomial expression for the particle angular scattering function. Their solution is included in Table 1 as HV87, after converting their quoted Legendre coefficients to double Henyey-Greenstein coefficients. However, the physical albedos derived from the Hapke model and the opposition magnitude do not match; therefore, the value of w was adjusted accordingly here which increased the formal geometric albedo (model HV87b).

7. Comparison of the photometric properties of Mercury and the Moon

The preferred solutions for the integral phase curves of Mercury (Sol. 1) and the Moon (Sol. 4) are presented in Fig. 4 together with observational data. These solutions are directly intercomparable since they have been determined with the same model (including the improvements in Hapke 2002) and obtained with the same fitting procedures. The solutions of other authors quoted in Table 1 are based on the Hapke (1986) formulation.

Relative to the Moon, the solutions of this work indicate that Mercury has a slightly lower single-scattering albedo, an opposition surge with smaller width and of marginally smaller amplitude, and a photometrically smoother surface. The width of the lobes of the single-particle scattering function is somewhat smaller for Mercury, and the backward scattering anisotropy is stronger. The same relationship is evident when contrasting the solutions of Mallama *et al.* (after adjusting c to 0.7 to conform to their Fig. 11 fit) with those of Helfenstein and Veverka (1987), except for the case of B_0 .

7.1. Absolute reflectances

The absolute reflectances of the two bodies may be readily compared by scaling their integral phase curves to the same cross-sectional disk area. In Fig. 5, the lunar V-band phase curve has been calibrated so that the physical size of the Moon is the same as Mercury's, and an interesting fact appears: on an absolute scale, the Moon is brighter than Mercury. Within the range of observational coverage for the two bodies, the Moon's average brightness (I/F) is 7–17% higher, with a possible minimum occurring at intermediate phase angles.

In a comparison such as this, careful calibration of the two data sets is crucial. The lunar photometry of Lane and Irvine (1973) is considered by Helfenstein and Veverka (1987) to be the most accurate available, and is used by them without corrections, as did Helfenstein *et al.* (1997). Regarding the details of the photometric calibration of Lane

and Irvine (1973), they state that "extensive observations of standard stars were made in order to define the color of the Sun in our observing system", and it is assumed that the calibration stars and procedures used are those of Irvine *et al.* (1968). The magnitudes of the secondary spectrophotometric standards employed were probably based on the then accepted absolute calibration of Vega. Hayes and Latham (1975) showed that the V-band magnitude of Vega in the then widely consulted Lick and Palomar absolute calibrations were wrong due to improper treatment of the atmospheric extinction. It is thus possible that the Lane and Irvine (1973) V-filter spectrophotometry of the Moon is too bright by up to 0.03 magnitudes.

The photometry of Rougier (1933) is for the wavelength 445 nm, while for Lane and Irvine (1973) and Mallama *et al.* (2002) the data is for the V-band (550 nm). In the conversion to V-band magnitude, neither Helfenstein and Veverka (1987) nor Helfenstein *et al.* (1997) corrected Rougier's magnitudes for the probable spectral reddening effect due to increasing phase angle. Lane and Irvine (1973) determined a difference in the lunar phase coefficient between these two wavelengths of about 0.001 mag/degree, with the V-band coefficient being smaller. Thus, the magnitude of the Moon increases more rapidly with phase angle in the V-band than at 445 nm. This effect can be seen, e.g., in Fig. 2 of Helfenstein *et al.* (1997), by contrasting the group of V-band data consisting of Shevchenko (1982) and Lane and Irvine (1973), to the group of 445 nm data of Rougier (1933) and Shorthill *et al.* (1969).

In the panel of Fig. 5, corrections for these two possible errors have been applied in order to show that they have negligible effect on the determination of a higher I/F value for the Moon than for Mercury. Fitting the corrected phase curve observations with 7-degree polynomials reveals that the I/F for the Moon is $\sim 15\%$ higher than for Mercury, and that the photometric scatter is small enough (1σ error of 4%) to place a high degree of confidence in this result. The result is thus model independent, and the difference in the average of the photometric observations for the two bodies is robust.

7.2. Albedos

With realization of the inherent uncertainties, the conclusion that Mercury is absolutely fainter than the Moon may be supported with the geometric albedo (p_V) values calculated from our fitted opposition $V(1,0)$ magnitudes, or from the best determinations of p_V of other authors (Tables 1 and 4). These indicate that the geometric albedo of the Moon is 11–12% higher than Mercury’s. As shown in Table 4 the determination of p_V for the Moon (Sol. 4) is slightly above those of other authors (e.g., Helfenstein and Veverka 1987, Veverka *et al.* 1988), and for Mercury in the high range of previously determined corresponding values (Veverka *et al.* 1988, Mallama *et al.* 2002). However, it should be remembered that the geometric albedo is very difficult to determine with any confidence unless the integral phase curve is constrained by observations down to very small phase angles which include the opposition surge. For the Moon, the opposition effect has been possible to quantify from orbiting spacecraft observations (e.g., Helfenstein *et al.* 1997), but for Mercury the effect is very poorly constrained, and the observations of Mallama *et al.* (2002) down to $\alpha = 2.2^\circ$ constitute the best source of information.

Hapke *et al.* (1975) determined a normal albedo A_n of 0.14 for the average Mercury at 554 nm wavelength based on Mariner 10 image data. This result assumed that the mercurian surface has the same photometric function as the Moon determined by Hapke (1966), and Hapke *et al.* (1975) state that due to this, ”actual uncertainties in the absolute albedos are probably of the order of 15%”. That a significant error in the absolute calibration of Mariner 10 data exists was shown by Mallama *et al.* (2002) who found that the intensity of a Mariner 10 brightness scan for a phase angle of 77° had to be decreased by 9% to conform to the brightness derived from the integral phase curve. It is similarly found here that a correction of -10% is necessary (Sec. 6) to fit the integral phase curve fit (Sol. 1) to latitudinal and longitudinal brightness profiles at phase angles of 77° and 106° . For the average near-side Moon, our solutions 4, 5 and 6 based on the integral phase curve predict the higher values $A_n = 0.149, 0.145,$ and 0.158 which are on average 10% greater

than for Mercury, in good accordance with results from both the geometric albedo and the ratio of the cross-section normalized integral phase curves out to 145° phase angle.

7.3. Hapke photometric parameters

In Fig. 9 the b and c parameters of the single-particle angular scattering function, determined from photometric observations of the integral Mercury and the Moon, are plotted relative to the locations of various experimental particles studied by McGuire and Hapke (1995). All solutions for the two bodies are located in the part of the diagram occupied by particles with a moderate to high density of internal scatterers, which are predominantly backward scattering and have rather wide scattering lobes. The positions of the solutions for Mercury are closer than the average Moon to that of complex particles with a large number of internal scatterers, and are more consistent with the scattering behavior of dark lunar maria than highlands. The scattering function of the average particle on Mercury’s surface appears to be both more backscattering and to have wider scattering lobes than the average Moon.

In the comparison of modelled and McGuire and Hapke’s experimental data, it should be noted that the latter were performed on artificial particles with size parameters $X \sim 50\,000$. The scattering properties of such particles may for this reason alone not be directly comparable to the natural particles expected on Mercury which appear to have an optically active average grain size of about $30\ \mu\text{m}$ ($X \sim 50$), about half the value for the Moon (Warell and Blewett 2003).

Helfenstein *et al.* (1997) performed a simultaneous fit of a modified Hapke photometric function over the phase angle range $0\text{--}144^\circ$, extended to include a description of the coherent backscatter effect, to the lunar V-filter disk-integrated phase curve and to disk-resolved images of average materials. They find parameter values (‘Solution 2a’) of $w = 0.279$, $h = 0.158$, $\bar{\theta} = 26.7^\circ$, and a primarily backscattering phase function with a

broad backscattering lobe and a narrower forward scattering lobe.

Hillier *et al.* (1999) determined Hapke photometric parameters from Clementine UV/Vis camera images at five wavelengths from 415 to 1000 nm, obtained at a phase angle range of 0–85°. Their model also accounted for coherent backscattering and used the same phase curve description as Helfenstein *et al.* (1997), but due to the restricted coverage in photometric geometry they could not determine the relative strength of the backward and forward lobes, the width of the forward lobe, or the surface roughness (these values were set to those determined by Helfenstein *et al.* 1997). The values of w for the average highlands and maria in the V-band (interpolated from their Table Va) are 0.43 and 0.27, at least as high as that for the average Moon of Helfenstein *et al.* (1997) and substantially higher than the mercurian and lunar values determined here.

The similarity in the derived values for h for the two bodies should also be noted. In contrast to Veverka *et al.* (1988), the different parameter solutions (Table 1, Sol. 1-6) indicate that the opposition surge may be somewhat smaller for Mercury, but the difference is not statistically significant. This indicates that the porosities of the average surfaces of Mercury and the near-side Moon are very similar.

The photometric surface roughnesses determined here are smaller than those determined previously by most other authors, both for Mercury and the Moon, especially when introducing the coherent backscatter contribution to the opposition effect. A small photometric roughness is required in order to increase the intensity of the integral phase curve to fit the high phase angle observations of Mercury. As is evident in Figs. 6 and 7, the slope angle is well bounded with values in the range $\sim 6 - 15^\circ$. Values for $\bar{\theta}$ in or above this range have been determined by previous authors from more limited (Danjon 1949) phase curve information (Hapke 1984, Veverka *et al.* 1988, Domingue *et al.* 1997, Mallama *et al.* 2002), and from narrow parameter searches based on disk-resolved Mariner 10 image data (Hapke 1984, Robinson and Lucey 1997). As is evident in Fig. 6, assigning lower weights to these observations, or attributing the large brightness to other causes

than photometric roughness, is required to allow a higher value for $\bar{\theta}$.

From mid-infrared observations of Mercury, Emery *et al.* (1998) determined a $\bar{\theta}$ value of 20° for near-equatorial longitudes of 10° – 75° and 100° – 160° , regions which are dominated by cratered and intercrater plains materials. From thermal infrared observations of the longitude range 210° – 250° (unimaged by Mariner 10), Sprague *et al.* (2000) found a considerably smaller surface roughness of 8 – 11° , possibly suggesting that the roughness varies over the surface.

Helfenstein and Veverka (1987) determined photometric roughnesses for lunar maria and highlands of 8° and 24° , respectively. The difference between these values was criticized by Helfenstein and Shepard (1999) as they could not easily be reconciled with the corresponding RMS slope angle distributions with size scale, measured from lunar regolith close-up images. They attributed this discrepancy to the inadequacy of the Hapke (1986) model to accurately retrieve absolute roughness values, specifically with respect to the representation of the employed particle angular scattering function and the non-inclusion of coherent backscattering. Incorporating these improvements, Helfenstein *et al.* (1997) determined a significantly larger surface roughness value of 27° for the average Moon.

Support for such a large photometric roughness for the Moon is found to be limited in the present work, though it is currently easier to allow a large roughness for the Moon than for Mercury due to the more restricted phase angle range for which lunar disk-integrated observations are presently available. Further observations of the lunar integral phase curve and the photometric properties of surface-resolved areas for phase angles $> 150^\circ$ are instrumental in resolving this question. Furthermore, extended multispectral observations of both bodies would provide the possibility to study the wavelength dependence of the Hapke parameters and from these constrain all model parameters. Increased understanding of the physical and light scattering properties of the surfaces of Mercury and the Moon will however be difficult to realize unless the photometric accuracy is also considerably improved.

8. Discussion

In this work, the best-calibrated sets of integral phase curve observations for Mercury and the Moon are intercompared. It is found that the near-side Moon, in the V-band, is of the order of 10–15% brighter than the average Mercury. This estimate is statistically significant at the 2σ level. This result is supported by the geometric albedos determined by all previous authors who have used reasonable photometric functions (Table 4). The general opinion appears to be the contrary, that Mercury is the brighter object. Perhaps, this arises from the flux calibration of the Mariner 10 vidicon camera (Hapke *et al.* 1975a), based on which it was concluded that the "heavily cratered plains have [normal] albedos of about 0.17, somewhat brighter than the lunar highlands", and that "albedos of the darker smooth plains and the interiors of bright fresh craters are systematically higher than their lunar counterparts". The average of the normal albedos of the first encounter incoming and outgoing hemispheres was determined to 0.14 for 554 nm wavelength and 5° phase angle. Furthermore, this value should be increased by about 30% to account for the opposition surge in order to be comparable to the geometric albedo at zero phase ($A_p=0.137$) determined from Earth-based observations. It is concluded here (as did Mallama *et al.* 2002) that the Mariner calibration is too bright by about 10% relative to Mercury's integral phase curve.

However, the fact that Mercury is fainter in the V-band does not imply that it is necessarily the absolutely brighter of the two bodies in terms of wavelength-integrated optical to near-infrared "bolometric" albedo, as the slope of Mercury's spectrum is considerable steeper than either lunar maria or highlands, even surpassing that of measured mature pure lunar anorthosites. This is due to the absence of a detectable mafic absorption band near $1\ \mu\text{m}$ for Mercury and the stronger state of maturation of its surface (Blewett *et al.* 2002, Warell 2003, Warell and Blewett 2003). Using the average geometric albedos presented in Table 4 to scale remotely sensed spectra (of Mare Serenitatis 2 from McCord *et al.* 1972, Apollo 12 from Melendrez *et al.* 1994, and Mercury from Warell and

Blewett 2003) for the wavelength range 400–1000 nm, the "bolometric" physical albedo of the Moon is found to be 0–5% higher than Mercury's.

Hapke (1999) makes a case that ground-based determinations of the absolute magnitudes of the planets may generally have errors of $\pm 10\%$ which may affect the above conclusion of the relative albedos of Mercury and the Moon, specifically when considering the difficult circumstances at which magnitude determinations of the former have to be performed. The ground-based photometry of Mallama *et al.* (2002) for Mercury is however in good accordance with the results from photometry from SOHO data, which strengthens the case that the photometry on average is of good quality. Accurate photometric measurements of the integral Moon may not be any easier to perform due to the large difference (as much as 15 magnitudes or more) between its brightness and that of the standard stars. To ultimately resolve this question, absolutely calibrated photometric measurements of both Mercury and the Moon in several well-defined wavelength bands, and of higher quality than is presently available, must be performed.

The improved integral phase curve for Mercury (Mallama *et al.* 2002) brings new important insight to the planet's photometric parameters. Specifically, it is found here that the only way to explain the bright high phase angle observations is to require a low value for the surface roughness, $\sim 8^\circ$. Limiting the phase angle range for Mercury increases the possibility of fitting larger surface roughness values to the integral phase curve data. Considering the lunar integral phase curve, and assuming that it does not behave very differently for high (unobserved) phase angles compared to Mercury's, leads to the conclusion that the surface roughness of the Moon may well be lower than what has been determined by most authors from the currently available phase angle coverage. Specifically, surface roughness values for the average Moon as high as 27° found by Helfenstein *et al.* (1997) are found to be difficult to reconcile with the high phase angle observations of its integral disk.

Brightness scans across the mercurian disk measured on Mariner 10 images (Hapke

1984, Mallama *et al.* 2002) are compared to different models (Fig. 10). Longitudinal profiles for two intermediate phase angles are properly fit with the parameter sets derived with methods *I* (Sol. 1–Sol. 3) and *II* (Sol. 7), after decreasing the Mariner 10 brightness by 10% to conform to integral phase curve observations. However, the models derived here predict a stronger limb darkening than observed for a brightness scan along a luminance meridian. To fit the Mariner data properly, a surface roughness of $\sim 15^\circ$ is required, but produces slightly worse fits for longitudinal brightness scans. There are different possible solutions to resolve this ambiguity in the value for $\bar{\theta}$: (i) the high phase angle observations of the integral phase curve are in error (though not considered as likely by Mallama *et al.* 2002); (ii) lowering the brightness of the observed profiles to less than that predicted from the integral phase curve would provide a consistent fit to $\bar{\theta} \sim 15^\circ$ models; (iii) there is a contribution, other than from the surface, to the integral brightness of Mercury at high phase angles; or (iv) the surface observed at $\alpha \sim 160 - 170^\circ$ is smoother than surfaces sampled at smaller phase angles. Of these, (iii) and (iv) merit further attention.

To fit a surface roughness of around 15° to the mercurian phase curve, the high phase angle observations must be fainter by 1–1.5 magnitudes. Mallama *et al.* (2002) discuss a possible intensity contribution due to the exosphere to explain the high brightness of the high phase angle observations. However, calculations by A. L. Sprague and D. Hunten (personal communication) indicate that this is not likely to be the case. Within the bandpass of the V filter, Na is the only known source of exospheric emission. At zero phase angle, the brightness of the exosphere is about 0.0005% of that of the surface within the bandpass. Since the Na atoms are excited by resonance scattering of surface-emitted photons, this number is roughly constant with phase angle, and the contribution is thus not important. This is true also for the case of a strongly backscattering phase function of the average mercurian surface, relative to the assumption of an isotropic resonance scattering phase function.

Brightness observations at phase angles greater than about 160° provide information

on the properties of only a minute portion of a planet’s surface, as the fraction of illuminated and visible disk is very small (of the order of 1% or less). This has important implications for the interpretation of the best-fit phase curve parameters, as in the worst case the properties of the sampled surface region may deviate greatly from the global average. The SOHO observations analyzed by Mallama *et al.* (2002) were obtained within a period of a few days at a lower conjunction at which surface regions close to the mercurian north pole reflected the observed light. The major contribution to the flux was provided by surface regions which are known (from Mariner 10 image data) to be dominated by smooth plains materials and lava-flooded impact basins. These regions include the Calorian age Borealis Planitia, the flooded 400-km size Tolstojan age Goethe crater and the lower latitude Calorian age Susei and Sobkou Planitia. The integral phase curve data for high phase angles thus appears dominated by macroscopically smooth surfaces, which may explain the observed high brightness of the disk. It is intriguing to note that a very low surface roughness of $\sim 8^\circ$ was determined by Helfenstein and Veverka (1987) for lunar maria, as this might provide independent support for the existence of similar surfaces on Mercury. However, disk brightness profiles from moderate phase angle Mariner 10 data are, on average, better interpreted with $\bar{\theta} \sim 15^\circ$.

Thus, to obtain integral phase curve data which is representative of the average mercurian surface, a much larger set of high-phase angle observations from SOHO should be analyzed. Such an exercise may show that the integral brightness of cratered surfaces and inter-crater plains are lower due to higher surface roughnesses. For a body with a photometrically heterogeneous surface on regional to global scales, a single satisfactory fit to phase angle brightness observations obtained at a singular apparition or spacecraft flyby may be difficult to obtain, as localized areas with varying surface textures are observed at different phase angles. This becomes increasingly true with increasing phase angle and would explain apparently discordant surface roughnesses for Mercury determined from separate integral phase curve and disk-resolved data sets.

To understand the physical implications of a small value of the subresolution-scale mean surface roughness angle derived from Hapke’s photometric theory, the small-scale structure of a regolith soil responsible for the macroscopic roughness perceived by remote sensing methods must be considered. Helfenstein and Shepard (1999) performed an in-depth study of high-resolution stereoscopic images of the undisturbed lunar regolith, and found that the measured macroscopic roughness is dominated by regolith structure at spatial scales of 0.1–80 mm, with only about 5% of the photometrically detected roughness being due surface relief at larger scales. At a scale of 1 mm, the average RMS amplitude of roughness (slope angle) for mare regoliths is around 16° , while for the surface most representative of highland units, the corresponding value is 25° . Thus the relative roughness ratio for highland compared to mare surfaces at this scale is about two. For the photometrically derived surface roughness, the difference between the two terrain types is smaller. Though decreasing average grain size is linked to increasing state of regolith maturation and increasing I_s/FeO maturity index (e.g., Langevin and Arnold 1977, Morris 1978), Helfenstein and Shepard (1999) could not find any clear dependence of the measured submillimeter-scale roughness on the maturity index. However, Shepard and Campbell (1998) found that the RMS slope angle increases with increasing photometric roughness. This implies that there may be a detectable difference in photometric roughness for these two surface types, though the constrained determination of $\bar{\theta}$ and w by Helfenstein and Shepard (1999) from disk-resolved lunar images indicate that the difference in photometric roughness values between highlands and maria would be small ($\bar{\theta} = 27^\circ$ and 24° , respectively). Thus, from an RMS slope angle viewpoint, a small value for the average photometric roughness on Mercury is consistent with the occurrence of wide-spread inviscid lava flows with smooth surfaces at sub-millimeter to sub-decimeter size scales.

Finally, it should be noted that a new photometric study of the Moon and Mercury may be valuable to perform when the phase function of the integrated near-side Moon, or of its individual surface types, has been determined for higher phase angles comparable to those available for Mercury. In such a scenario, a more complex phase function than

the 2-term Henyey-Greenstein function may or may not provide additional support for the low values of their surface roughnesses determined here. This is due to the fact that, with a higher-order particle phase function, it will be possible to determine the widths and magnitudes of the backward and forward scattering lobes separately. It has been shown (e.g., McGuire and Hapke 1995) that naturally occurring regolith particles tend to have broad and low backscattering lobes, and narrow and high forward lobes. This behaviour cannot be adequately reproduced by the 2-term Henyey-Greenstein function which enforces the same widths and magnitudes for both lobes. The use of a phase function representation with individual treatment of the scattering lobes may show that small values for the photometric surface roughness angle is related to the fact that the 2-term Henyey-Greenstein function determines too small values for the magnitude of the forward scattered lobe in order to compensate for a smaller magnitude, wider backscattering lobe. If and when lunar phase curve data with considerably extended phase angle range becomes available, an improved comparative study between Mercury and the Moon will be possible to perform to address these issues.

Acknowledgements

Ann Sprague and Bruce Hapke are thanked for helpful comments and discussions during the course of this work. Paul Helfenstein and John Kenneth Hillier provided valuable reviews which improved the paper. The Swedish Vacuum Solar Telescope is operated on the island of La Palma by the Institute for Solar Physics of the Royal Swedish Academy of Sciences in the Spanish Observatorio del Roque de los Muchachos of the Instituto de Astrofísica de Canarias.

References

- Blewett, D. T., B. R. Hawke and P. G. Lucey 2002. Lunar pure anorthosite as a spectral analog for Mercury. *Meteorit. Planet. Sci.* **37**, 1245–1254.
- Bowell, E., B. Hapke, D. Domingue, K. Lumme, J. Peltoniemi, and A. W. Harris 1989. Application of photometric models to asteroids. In: Binzel, R., Gehrels, T., Matthews, M. S. (Eds.), *Asteroids II*, Univ. of Arizona Press, Tucson, pp. 525–556.
- Buratti, B. J., J. K. Hillier, and M. Wang 1996. The lunar opposition surge: Observations by Clementine. *Icarus* **124**, 490–499.
- Danjon, A. 1949. Photometrie et Colorimetrie des Planètes Mercure et Venus. *Bull. Astron. J.* **14**, 315.
- De Vaucouleurs, G. 1964. Geometric and photometric properties of the terrestrial planets. *Icarus* **3**, 187–235.
- Dollfus, A. and M. Auriere 1974. Optical polarimetry of planet Mercury. *Icarus* **23**, 465–482.
- Domingue, D. and B. Hapke 1989. Fitting Theoretical Photometric Functions to Asteroid Phase Curves. *Icarus* **78**, 330–336.
- Domingue, D. L., A. L. Sprague, and D. M. Hunten 1997. Dependence of Mercurian Atmospheric Column Abundance Estimations on Surface-Reflectance Modeling. *Icarus* **128**, 75–82.
- Emery, J. P., A. L. Sprague, F. C. Witteborn, J. E. Colwell, R. W. H. Kozlowski, and D. H. Wooden 1998. Mercury: Thermal Modeling and Mid-Infrared (5–12 μm) Observations. *Icarus* **136**, 104–123.
- Hapke, B. 1966. An improved theoretical lunar photometric function. *Astron. J.* **71**, 333–339.

- Hapke, B., G. E. Danielson, K. Klaasen, and L. Wilson 1975. Photometric Observations of Mercury From Mariner 10. *J. Geophys. Res.* **80**, 2431–2443.
- Hapke, B. 1981. Bidirectional reflectance spectroscopy I. Theory. *J. Geophys. Res.* **86**, 3039–3054.
- Hapke, B. 1984. Bidirectional reflectance spectroscopy III. Correction for macroscopic roughness. *Icarus* **59**, 41–59.
- Hapke, B. 1986. Bidirectional reflectance spectroscopy IV. The extinction coefficient and the opposition effect. *Icarus* **67**, 264–281.
- Hapke, B. 1993. *Theory of reflectance and emittance spectroscopy*. Cambridge University Press, Cambridge.
- Hapke, B. 1999. Scattering and diffraction of light by particles in planetary regoliths. *J. Quant. Spectrosc. Radiat. Transfer* **61**, 565–581.
- Hapke, B. 2002. Bidirectional Reflectance Spectroscopy. 5. The Coherent Backscatter Opposition Effect and Anisotropic Scattering. *Icarus* **157**, 523–534.
- Harris, D.L. 1961. Photometry and colorimetry of planets and satellites. In: Kuiper, G.P., Middlehurst, B. M. (Eds.), *Planets and Satellites*, vol. 3, University of Chicago Press, Chicago.
- Hartman, B., and D. Domingue 1998. Scattering of Light by Individual Particles and the Implications for Models of Planetary Surfaces. *Icarus* **131**, 421–448.
- Hayes, D. S., and D. W. Latham 1975. A rediscussion of the atmospheric extinction and the absolute spectral-energy distribution of Vega. *Astrophys. J.* **197**, 593–601.
- Helfenstein, P. and J. Veverka 1987. Photometric properties of lunar terrains derived from Hapke's equation. *Icarus* **72**, 342–357.

- Helfenstein, P. and J. Veverka 1989. Physical characterization of asteroid surfaces from photometric analysis. In: Binzel, R., Gehrels, T., Matthews, M. S. (Eds.), *Asteroids II*, Univ. of Arizona Press, Tucson, pp. 557–593.
- Helfenstein, P., J. Veverka, and J. Hillier 1997. The Lunar Opposition Effect: A Test of Alternative Models. *Icarus* **128**, 2–14.
- Helfenstein, P., and M. K. Shepard 1999. Submillimeter-Scale Topography of the Lunar Regolith. *Icarus* **141**, 107–131.
- Hillier, J. K., B. B. Buratti, and K. Hill 1999. Multispectral Photometry of the Moon and Absolute Calibration of the Clementine UV/Vis Camera. *Icarus* **141**, 205–225.
- Irvine, W. M., T. Simon, D. H. Menzel, C. Pikoos and A. T. Young 1968. Multicolor Photoelectric Photometry of the Brighter Planets. III. Observations from Boyden Observatory. *Astron. J.* **73**, 807–828.
- Kreslavsky, M. A., Yu. G. Shkuratov, Yu. I. Velikodsky, V. G. Kaydash, and D. G. Stankevich 2000. Photometric properties of the lunar surface derived from Clementine observations. *J. Geophys. Res.* **105** (E8), 20 281–20 295.
- Lane, A. P. and W. M. Irvine 1973. Monochromatic phase curves and albedo for the lunar disk. *Astron. J.* **78**, 267–277.
- Langevin, Y., and J. R. Arnold 1977. The evolution of the lunar regolith. *Ann. rev. Earth Planet. Sci.* **5**, 449–489.
- Lumme, K. and E. Bowell 1981a. Radiative transfer in the surfaces of atmosphereless bodies. I. Theory. *Astron. J.* **86**, 1694–1704.
- Lumme, K. and E. Bowell 1981b. Radiative transfer in the surfaces of atmosphereless bodies. II. Interpretation of phase curves. *Astron. J.* **86**, 1705–1721.

- Lumme, K. and W. M. Irvine 1982. Radiative transfer in the surfaces of atmosphereless bodies. III - Interpretation of lunar photometry. *Astron. J.* **87**, 1076–1082.
- Mallama, A., D. Wang, and R. A. Howard 2002. Photometry of Mercury from SOHO/LASCO and Earth. *Icarus* **155**, 253–264.
- McCord, T. B., M. P. Charette, T. V. Johnson, L. A. Lebofsky, C. M. Pieters, and J. B. Adams 1972. Lunar Spectral Types. *J. Geophys. Res.* **77**, 1349–1359.
- McGuire, A. F. and B. W. Hapke 1995. An Experimental Study of Light Scattering by Large, Irregular Particles. *Icarus* **113**, 134–155.
- Melendrez, D. E., J. R. Johnson, S. M. Larson, and R. B. Singer 1994. Remote sensing of potential lunar resources. 2. High spatial resolution mapping of spectral reflectance ratios and implications for nearside mare TiO₂ content. *J. Geophys. Res.* **99** (E3), 5601–5619.
- Morris, R. V. 1978. The surface exposure (maturity) of lunar soils: Some concepts and I_s/FeO compilation. *Proc. Lunar Planet Sci. Conf., 9th*, 2287–2297.
- Nikonova, E. K. 1949. *Izv. Krymskoi Astrofiz. Obs.* **4**, 114.
- Robinson, M. S., and P.G. Lucey 1997. Recalibrated Mariner 10 image mosaics: Implications for Mercurian volcanism. *Science* **275**, 197–200.
- Russell, H. N. 1916. On the albedo of planets and their satellites. *Astrophys. J.* **43**, 173.
- Rougier, G. 1933. Photometrie photoelectrique global de la Lune. *Ann. Obs. Strasbourg* **2**, 205–399.
- Shepard, M. K, and B. A. Campbell 1998. Shadows on a Planetary Surface and Implications for Photometric Roughness. *Icarus* **134**, 279–291.

- Shevchenko, V. V. 1982. The lunar photometric constants in the system of the true full Moon. In: Fricke, W., Teleki, G. (Eds.), *The Sun and Planetary System*, Reidel, Dordrecht, pp. 263–264.
- Shkuratov, Yu. G., M. A. Kreslavsky, A. A. Ovcharenko, E. S. Zubko, C. Pieters, and G. Arnold 1999a. Opposition effect from Clementine Data and Mechanisms of Backscatter. *Icarus* **141**, 132–155.
- Shkuratov, Yu., L. Starukhina, H. Hoffmann, and G. Arnold 1999b. A Model of Spectral Albedo of Particulate Surfaces: Implications for Optical Properties of the Moon. *Icarus* **137**, 235–246.
- Shorthill, R. W., J. M. Saari, F. E. Baird, and J. R. LeCompte 1969. *Photometric Properties of Selected Lunar Features*. NASA Contractor Report CR-1429.
- Sprague, A. L., L. K. Deutsch, J. Hora, G. G. Fazio, B. Ludwig, J. Emery, and W. F. Hoffmann 2000. Mid-Infrared (8.1–12.5 μm) Imaging of Mercury. *Icarus* **147**, 421–432.
- Veverka, J., Helfenstein, P., Hapke, B. and J. Goguen 1988. Photometry and polarimetry of Mercury. In: Vilas, F., Chapman, C. R., Matthews, M. S. (Eds.), University of Arizona Press, Tucson, pp. 37–58.
- Warell, J. and S. S. Limaye 2001. Properties of the Hermean regolith: I. Global regolith albedo variation at 200 km scale from multicolor CCD imaging. *Planet. Space Science* **49**, 1531–1552.
- Warell, J. 2002. Properties of the Hermean regolith: II. Disk-resolved multicolor photometry and color variations of the "unknown" hemisphere. *Icarus* **156**, 303–317.
- Warell, J. 2003. Properties of the Hermean regolith: III. Disk-resolved vis-NIR reflectance spectra and implications for the abundance of iron. *Icarus*, **161**, 199–222.

Warell, J. and D. T. Blewett 2003. Properties of the Hermean regolith: V. New optical reflectance spectra, comparison with lunar anorthosites, and mineralogical modelling. Submitted to *Icarus*.

Table 1. V-band photometric parameters of Mercury and the Moon (Method I)

Note: Sources V88, B89, D97, and H87 denote Veverka *et al.* (1988), Bowell *et al.* (1989) and Domingue *et al.* (1997) (who used Danjon (1949) phase curve data), and Helfenstein and Veverka (1987) (who used Russell (1916), Rougier (1933), and Shorthill *et al.* (1969) phase curve data), respectively. The M02 fit is too faint at high α . The H87 model was adjusted here to bring the Hapke modelled p_V in line with that obtained from $V(1,0)$ and presented as model H87b. The b and c parameter values from sources other than this work have been converted from three-term Legendre polynomial coefficients to double Henyey-Greenstein coefficients. Error ranges for Sol. 1–6 parameters reflect the maximal parameter variations that, when varied individually, produce fits within the observational scatter. The quoted RMS value is for the nominal solution. Sol. 1 and Sol. 4 are the preferred solutions of this work.

w	b	c	h	B_0	$\bar{\theta}$ ($^\circ$)	$V(1,0)$	p_V	q_V	A_V
<i>Mercury</i>									
0.160±0.001	0.18±0.02	1.1±0.2	0.09±0.02	2.7 $^{+0.8}_{-0.4}$	8±1	-0.65±0.02	0.136±0.005	0.458±0.004	0.063±0
0.172±0.001	0.18±0.02	1.3±0.2	0.09±0.02	2.2 $^{+0.8}_{-0.4}$	7±1	-0.64±0.02	0.135±0.005	0.488±0.004	0.066±0
0.179±0.001	0.17 $^{+0.01}_{-0.02}$	0.85 $^{+0.1}_{-0.2}$	0.08±0.02	2.8 $^{+0.5}_{-0.4}$	16 $^{+2}_{-3}$	-0.68±0.02	0.140±0.005	0.443±0.004	0.062±0
0.20	0.19	0.35	0.065±0.002	2.4	16±1	-0.69±0.03	0.142±0.005	0.478±0.004	0.068±0
0.20	0.19	0.35	0.11	2.4	21	–	0.140	0.473	0.
0.23	0.17	0.35	0.09	2.5	25	–	0.138	0.486	0.
0.21	0.28	0.47	0.03	1.85	20	–	–	–	0.
0.20	0.19	0.35	0.11	2.4	21	–	–	–	0.
0.23	0.17	0.35	0.09	2.5	25	–	–	–	0.
<i>Moon</i>									
0.168±0.001	0.21±0.02	0.7±0.1	0.11±0.03	3.1±0.5	11 $^{+3}_{-4}$	-0.03±0.02	0.152±0.005	0.452±0.004	0.068±0
0.159	0.18	0.5	0.15	4.0	15	+0.02	0.148	0.482	0.
0.242	0.20	0.3	0.07	2.7	25	-0.11	0.163	0.423	0.
0.21	0.40	0.60	0.07	2.0	20	–	0.136	0.451	0.
0.244	0.40	0.60	0.07	2.0	20	-0.08	0.159	0.457	0.

Table 2. V-band photometric parameters of Mercury obtained from disk-resolved image profiles with phase curve constraint (Method II)

Note: Image brightnesses calibrated to the V-band. * Relative to integral phase curve. The average solution is "Sol. 7".

Date	Im. No.	w	b	c	h	B_0	$\bar{\theta}$ ($^\circ$)	$V(1,0)$	p_V
1995 Oct 22	245	0.16 ± 0.02	0.16 ± 0.04	1.4 ± 0.4	0.07 ± 0.03	2.8 ± 0.5	7 ± 2	-0.79	0.15
	248	0.16 ± 0.02	0.20 ± 0.02	1.2 ± 0.3	0.06 ± 0.03	2.6 ± 0.6	7 ± 2	-0.64	0.13
	257	0.16 ± 0.02	0.19 ± 0.04	1.4 ± 0.4	0.06 ± 0.03	2.3 ± 0.4	6 ± 3	-0.66	0.14
1997 Nov 24	48	0.15 ± 0.03	0.17 ± 0.05	1.2 ± 0.5	0.07 ± 0.04	3.0 ± 0.7	8 ± 2	-0.67	0.14
	193	0.17 ± 0.02	0.19 ± 0.05	1.1 ± 0.4	0.07 ± 0.03	3.0 ± 0.7	9 ± 2	-0.75	0.14
1998 Jul 9	117	0.15 ± 0.02	0.17 ± 0.05	1.4 ± 0.5	0.09 ± 0.04	2.9 ± 0.5	6 ± 3	-0.70	0.13
	167	0.13 ± 0.03	0.16 ± 0.07	1.3 ± 0.6	0.11 ± 0.05	3.4 ± 1.1	8 ± 3	-0.61	0.11
1999 Apr 27	154	0.12 ± 0.03	0.18 ± 0.03	1.0 ± 0.4	0.11 ± 0.04	3.3 ± 1.1	8 ± 3	-0.65	0.10
	155	0.16 ± 0.03	0.21 ± 0.06	1.1 ± 0.5	0.06 ± 0.03	2.6 ± 0.7	8 ± 3	-0.62	0.11
<i>Average $\pm 1\sigma$ (Sol. 7)</i>		0.15 ± 0.02	0.18 ± 0.02	1.2 ± 0.2	0.08 ± 0.02	2.9 ± 0.4	7 ± 1	$-0.67\pm 0.02^*$	0.140 ± 0.017

Table 3. Photometric parameters for disk-resolved images of Mercury (Method *III*)

Note: Parameters were derived with the constraints $b = 0.18$, $c = 1.2$, $h = 0.08$, and $B_0 = 2.9$ (Table 2) and flux scaling with wavelength according to the disk-integrated relative geometric albedo of Warell (2002).

Date	Im. No.	α ($^\circ$)	λ (nm)	σ ($''$)	w	$\bar{\theta}$	RMS
1995 Oct 22	245	75.9	543	0.25	0.152 \pm 0.006	9 \pm 3	.00067
(lon. 269 $^\circ$ –13 $^\circ$)	248	75.9	543	0.25	0.153 \pm 0.005	9 \pm 4	.00077
	190	75.9	790	0.45	0.193 \pm 0.007	5 \pm 3	.00071
	210	75.9	875	0.40	0.223 \pm 0.006	3 \pm 2	.0011
1996 Apr 19	82	89.4	753	0.25	0.199 \pm 0.006	8 \pm 5	.00036
(lon. 2 $^\circ$ –92 $^\circ$)	83	89.4	753	0.25	0.199 \pm 0.006	8 \pm 5	.00033
1997 Nov 24	193	63.4	554	0.35	0.164 \pm 0.006	15 \pm 4	.0011
(lon. 133 $^\circ$ –249 $^\circ$)	48	63.4	650	0.25	0.205 \pm 0.005	16 \pm 3	.0015
	80	63.4	753	0.30	0.232 \pm 0.007	15 \pm 4	.0011
	115	63.4	833	0.33	0.241 \pm 0.005	11 \pm 3	.0018
1998 Jul 9	117	84.0	554	0.28	0.143 \pm 0.006	6 \pm 5	.00044
(lon. 218 $^\circ$ –313 $^\circ$)	167	84.0	650	0.30	0.163 \pm 0.004	7 \pm 3	.00031
	209	84.0	753	0.35	0.189 \pm 0.007	9 \pm 5	.00026
	66	84.0	833	0.33	0.210 \pm 0.006	13 \pm 3	.00059
	246	84.0	944	0.40	0.227 \pm 0.006	12 \pm 3	.00064
1999 Apr 27	155	75.6	650	0.30	0.176 \pm 0.008	11 \pm 6	.00076
(lon. 44 $^\circ$ –148 $^\circ$)							
<i>Average $\pm 1\sigma$</i>						10 \pm 4	

Table 4. Determinations of V-band geometric albedos for Mercury and the integral Moon

Note: Abbreviations are B89 (Bowell *et al.* 1989), D49 (Danjon 1949), D74 (Dollfus and Auriere 1974), D74 (de Vaucouleurs 1974), H61 (Harris 1961), H86 (Hapke 1986), H87 (Helfenstein and Veverka 1987), H93 (Hapke 1993), H02 (Hapke 2002), L73 (Lane and Irvine 1973), L81a (Lumme and Bowell 1981a), L81b (Lumme and Bowell 1981b), L82 (Lumme and Irvine 1982), M02 (Mallama *et al.* 2002), N49 (Nikonova 1949), R16 (Russell 1916), R33 (Rougier 1933), S69 (Shorthill 1969), S82 (Shevchenko 1982), V88 (Veverka *et al.* 1988), OE (opposition effect). Observations of Rougier (1933) and Shorthill *et al.* (1969) are for 445 nm (corrected to V, neglecting possible phase reddening), others for the V-band (550 nm).

p_V	Min. α ($^\circ$)	Author, solution	Source of photometry	Model type	Comment
<i>Mercury</i>					
0.125	3.0	M02	D49	7 $^\circ$ pol.	
0.115	3.0	H61	D49	3 $^\circ$ pol.	
0.109	3.0	D64	D49	3 $^\circ$ pol.	Recalibration by M02
0.130	4.5	D74	D74	(Best fit)	Polarimetric, for $\alpha = 5^\circ$
0.130	3.0	L81b	D49	L81a	Fit restricted to $\alpha < 25^\circ$
0.139	3.0	V88, sol. 1	D49	H86	
0.137	3.0	V88, sol. 2	D49	H86	
0.140	3.0	B89	D49	H86	
0.142	2.2	M02	M02	H93	
0.136	2.2	Sol. 1	M02	H02	This work
0.135	2.2	Sol. 2	M02	H02	This work
0.140	2.2	Sol. 3	M02	H02	This work
0.132 ± 0.011 ($N=12$)					<i>Average (1σ error)</i>
0.137 ± 0.004 ($N=8$)					<i>Ave. neglecting first four</i>
0.137 ± 0.003 ($N=3$)					<i>Average, this work only</i>
<i>Moon</i>					
0.113	6.6	L73	L73	Linear fit	OE neglected
0.152	6.6	L82	L73	L81a	
0.147	1.4	S82	R33, N49	3 $^\circ$ pol.	
0.136	2.3	H87	R16,R33,S69,L73	H86	
0.152	2.4	Sol. 4	R33, L73	H02	This work
0.148	2.4	Sol. 5	R33, L73	H02	This work
0.163	2.4	Sol. 6	R33, L73	H02	This work
0.144 ± 0.016 ($N=7$)					<i>Average (1σ error)</i>
0.150 ± 0.009 ($N=6$)					<i>Average neglecting L73</i>
0.154 ± 0.008 ($N=3$)					<i>Average, this work only</i>

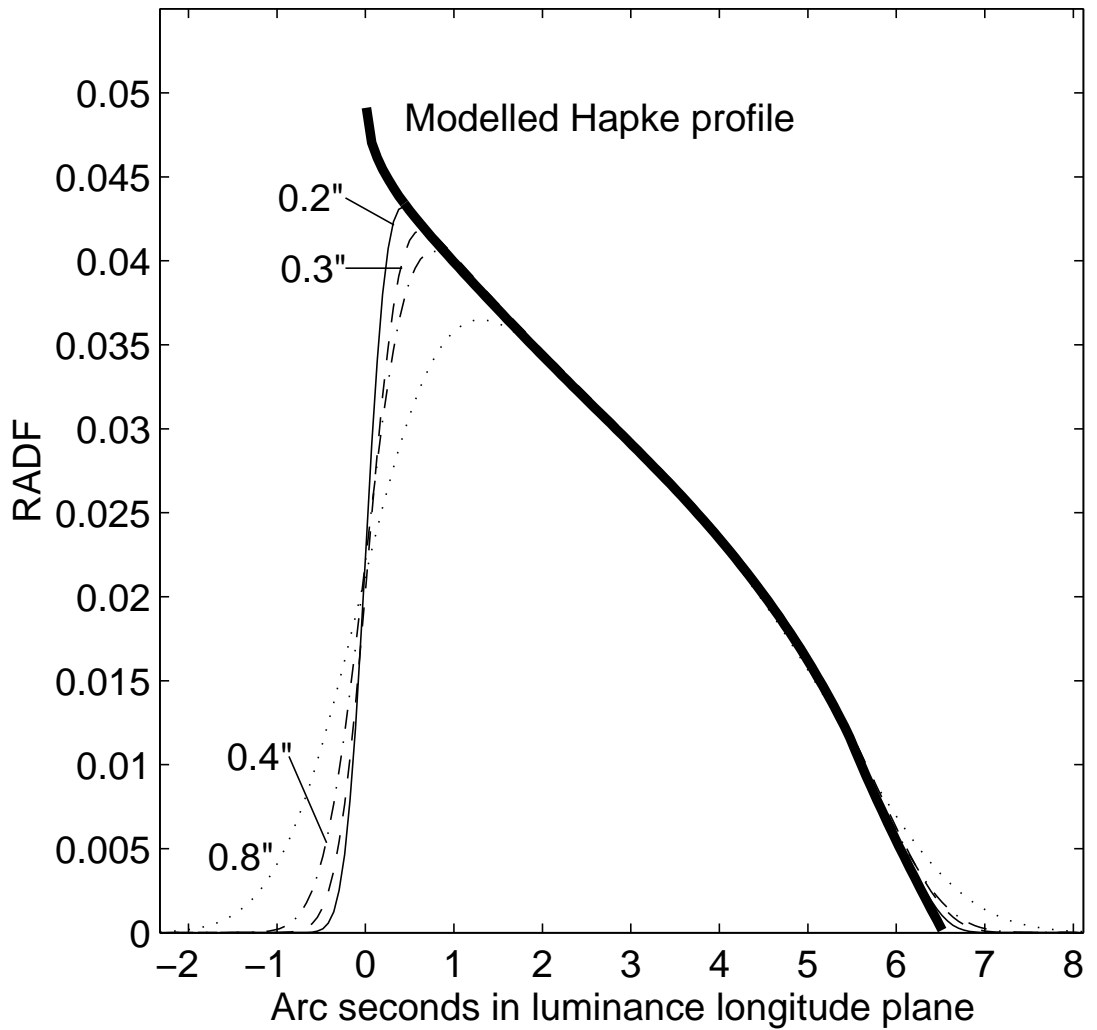


Fig. 1.— Effect on the shape of the intensity profile along the luminance equator of a Mercury model convolved with Gaussians of various widths to simulate seeing smear of the observed Mercury disk. The modelled profile is based on the Hapke parameters of Robinson and Lucey (1997) for the Earth-based geometry of Mercury on November 24, 1997, at a phase angle of 63° . The disk profile has been convolved with Gaussians of effective FWHM diameters of 0.2, 0.3, 0.4, and $0.8''$. The diffraction limited resolution at 550 nm for the SVST is $0.25''$, while the maximum seeing smear for any of the images used in the analysis is adequately modelled by a $0.4''$ wide Gaussian. Intensity is in radiance factor units (πr).

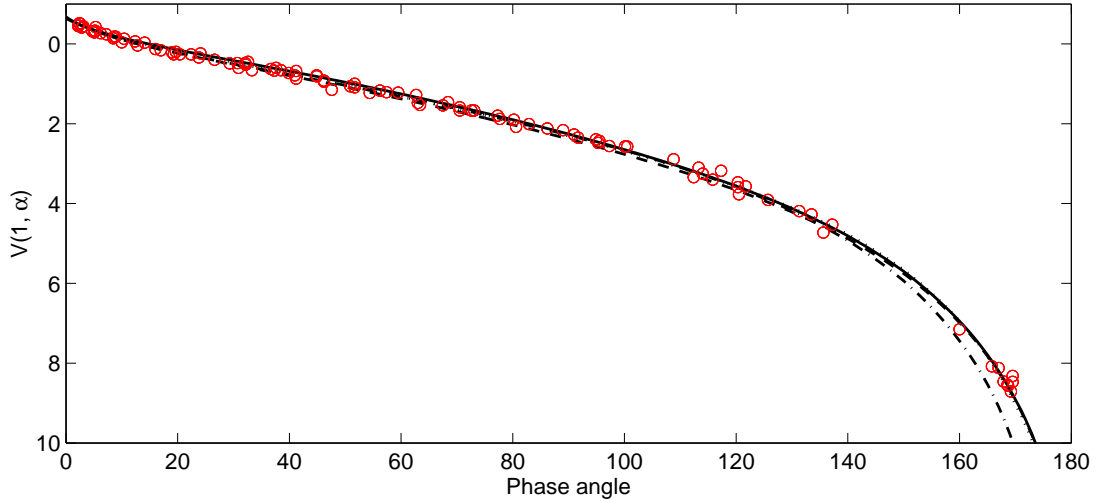


Fig. 2.— The V-band integral phase curve observations of Mallama *et al.* (2002) fitted with Hapke parameter sets determined in this work. The dash-dotted solution (Sol. 3) is based on phase curve observations to $\alpha < 145^\circ$ and is too faint at higher phase angles, similar to the solutions 1 and 2 of Veverka *et al.* (1988) and 1–3 of Domingue *et al.* (1997) which are fitted to the observations of Danjon (1949), extending to $\alpha = 123^\circ$. To fit the observations at $160^\circ < \alpha < 170^\circ$, a photometrically smoother and more backscattering surface is required. Such solutions have $\bar{\theta} \sim 8^\circ$ and are illustrated with dotted and solid lines (Sol. 1 and Sol. 2, respectively, based on integral phase curve data only) and a dashed line (Sol. 7, based on disk-resolved ground-based image brightness profiles constrained by the phase curve). These three solutions nearly overlap throughout the full range of phase angles.

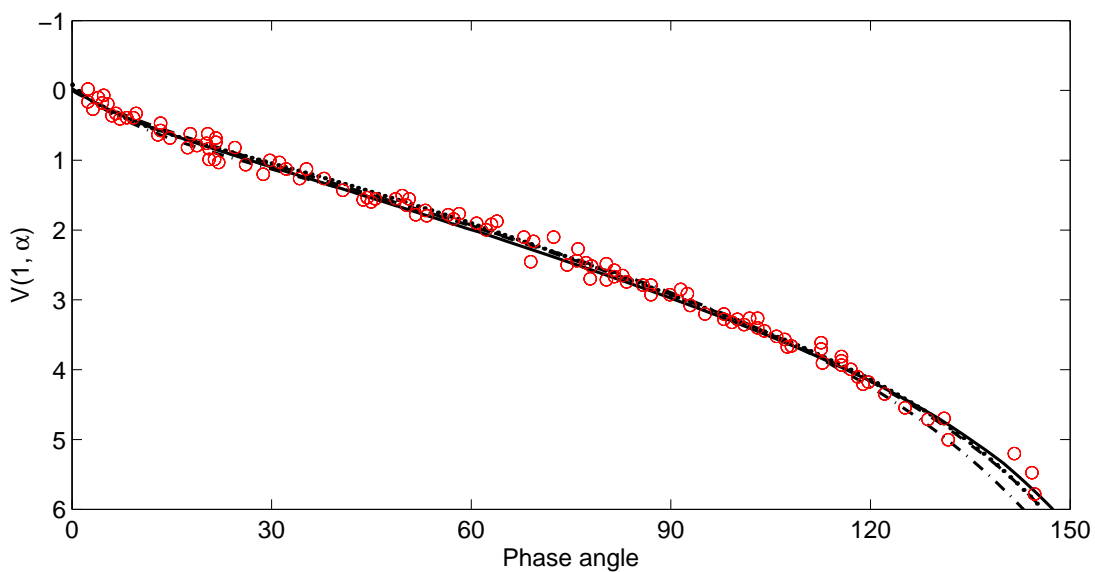


Fig. 3.— Model fits to the lunar phase curve observations of Rougier (1933), calibrated to V-band brightness. The best-fit solution is Sol. 4 (solid line) which has a surface roughness of 11° . Solutions Sol. 5 and Sol. 6 are shown as dashed and dot-dashed lines respectively, while the solution of Helfenstein and Veverka (1987; overlapping "Sol. 5" at the highest phase angles) is represented by a dotted line.

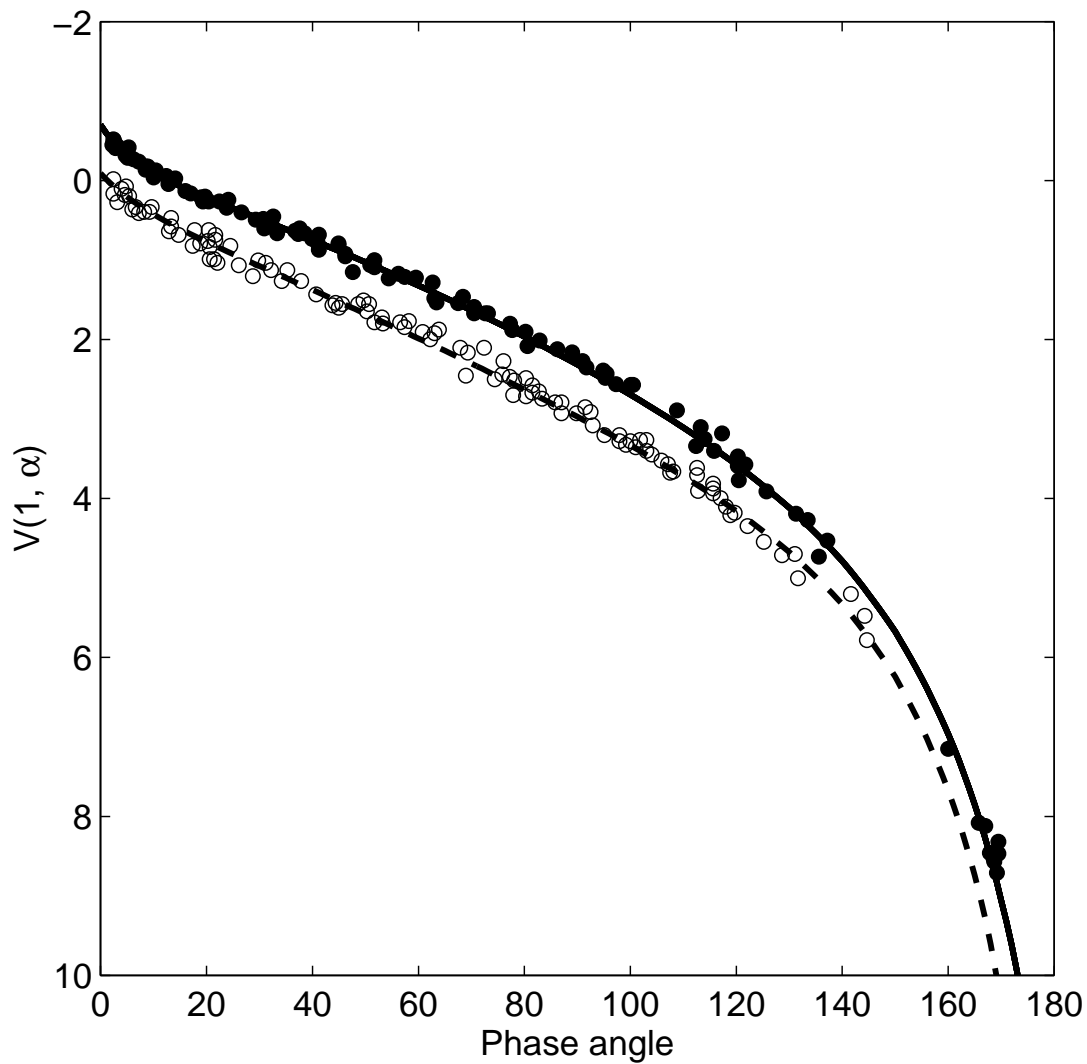


Fig. 4.— Optimal fits to the integral phase curves of Mercury (Sol. 1, solid line) and the Moon (Sol. 4, dashed line) based on V-filter observations of Mallama *et al.* (2002; filled circles) and Rougier (1933; open circles, calibrated to V-band brightness), respectively.

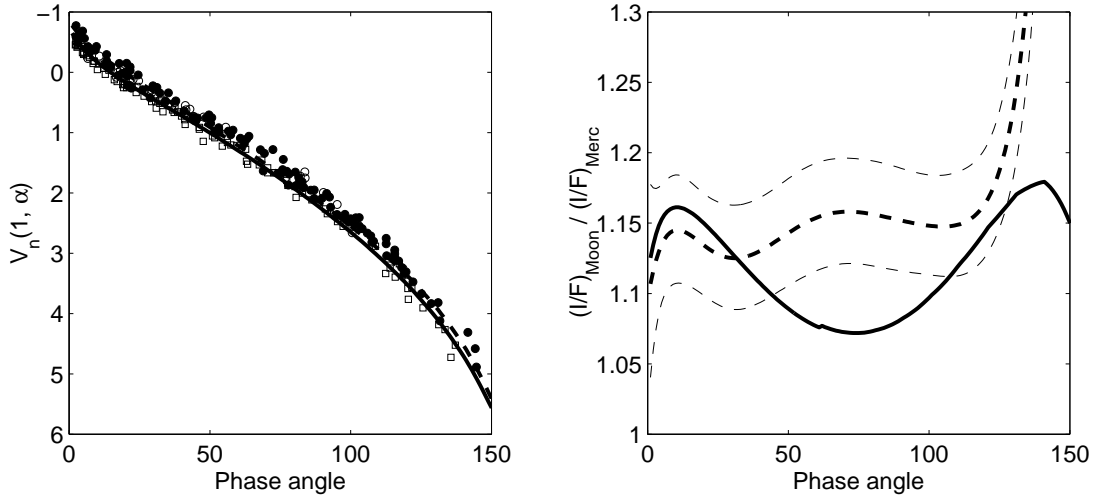


Fig. 5.— Left: The integral phase curves of Mercury (solid line) and the Moon (dashed line), normalized to the cross-sectional area of Mercury. The lunar phase curve is unconstrained for phase angles larger than 144° . Right: The intensity of the normalized phase curve of the Moon divided by that of Mercury (solid line). The dashed line with 1σ error envelope is the ratio of the phase curve data fit with 7-degree polynomials, corrected for possibly incorrect absolute calibration of the Lane and Irvine (1973) observations, and the expected amount of phase reddening. For the common range of observational coverage ($2\text{--}144^\circ$), the brightness of the Moon is 7–17% higher than Mercury’s.

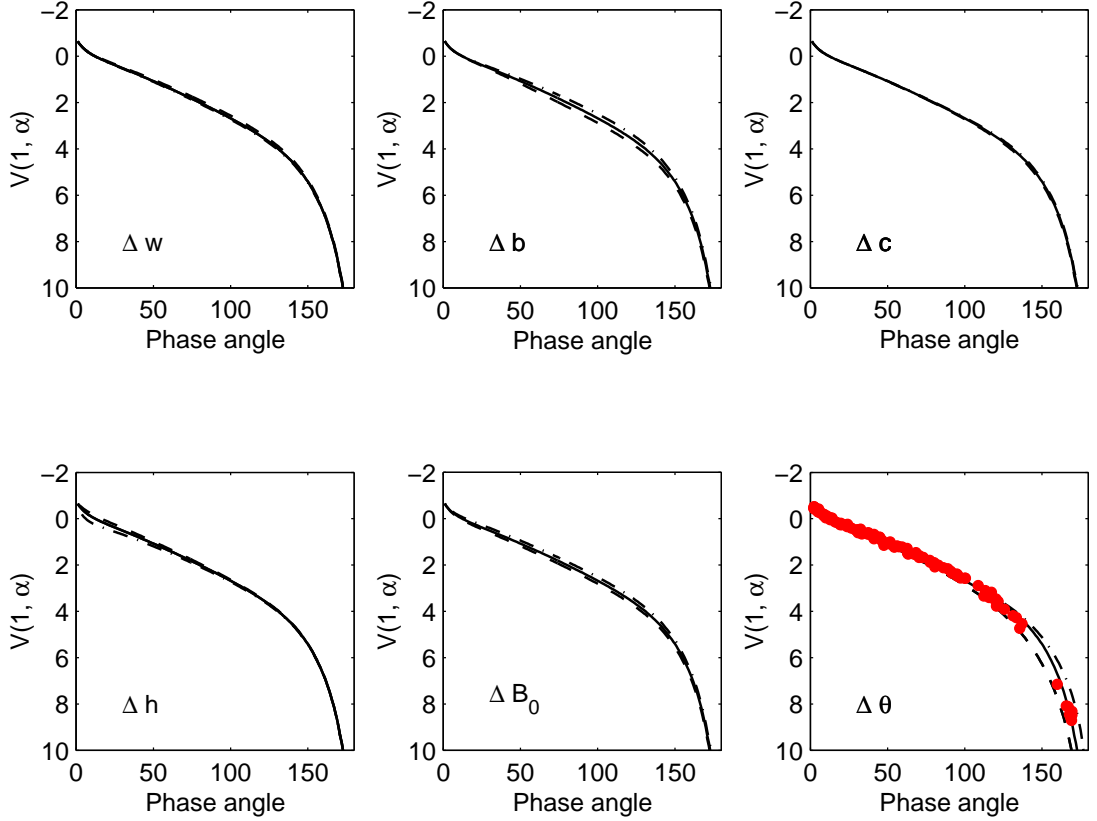


Fig. 6.— Effects on the phase curve of individual variations of the Hapke parameter values relative to the nominal fit for Mercury (Sol. 1, cf. Fig. 2). The single-particle scattering albedo and the subresolution-scale mean surface roughness angle are varied between half and twice the values given for Sol. 1 (Table 1), while for the other parameters the variation is 2σ . The solution with a higher parameter value is shown by a dashed line, while the solution with a lower value is a dot-dashed line. In the case of w and h a smaller parameter value lowers the intensity of the phase curve, while the effect is opposite for the other parameters. In the lower right panel the observations of Mallama *et al.* (2002) used in the fitting procedure are shown.

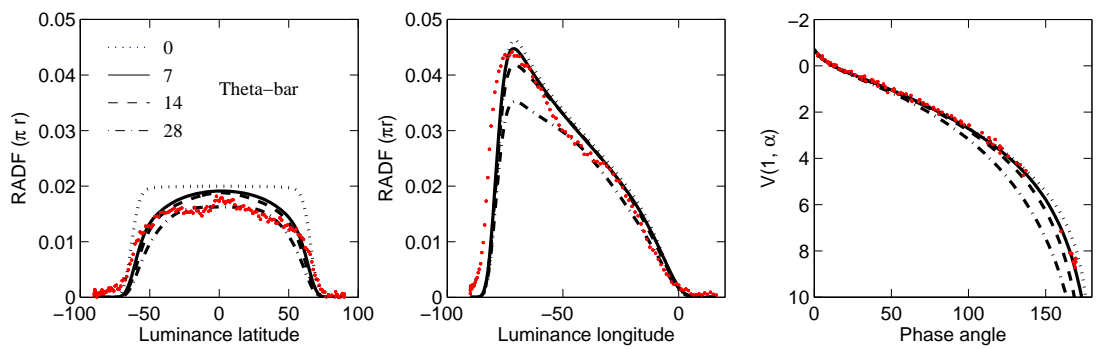


Fig. 7.— Typical result of fitting the Hapke photometric model (solid lines) simultaneously to observational data (dots) in the form of central meridian and luminance equator disk profiles (left and central panels, respectively) and the Mallama *et al.* (2002) integral phase curve (right panel), for varying values of $\bar{\theta}$. These profiles are for the 550 nm image #245, obtained with the SVST at $0.25''$ seeing conditions (cf. Table 2).

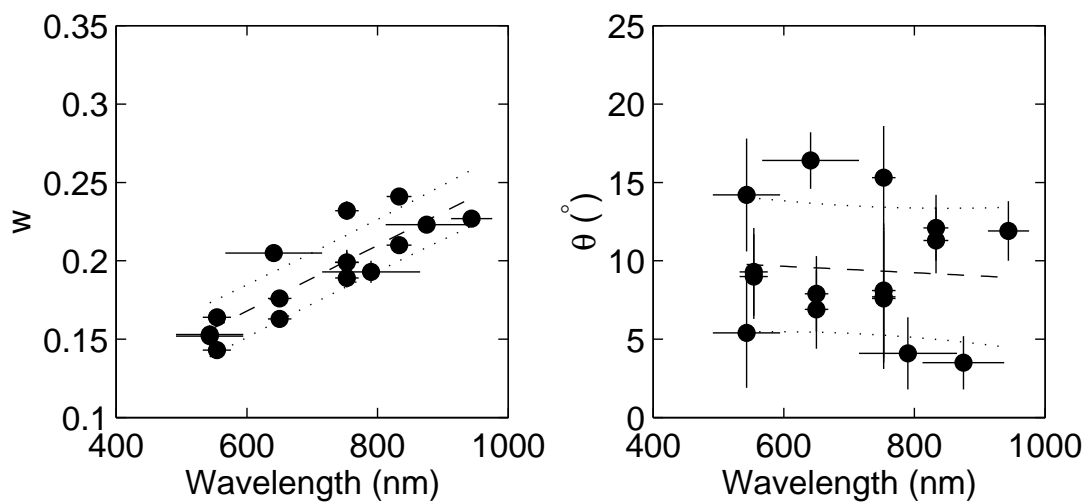


Fig. 8.— single-particle scattering albedo w and photometric surface roughness angle $\bar{\theta}$ for Mercury plotted as a function of wavelength. These values were obtained by constraining b , c , h , and B_0 to the values determined at 550 nm with method *II* (Table 2). Dashed lines are linear least squares fits to the data, dotted lines indicate 1σ error envelopes. Both relations show the expected behavior; w increases with wavelength, while the average value of $\bar{\theta}$ is constant.

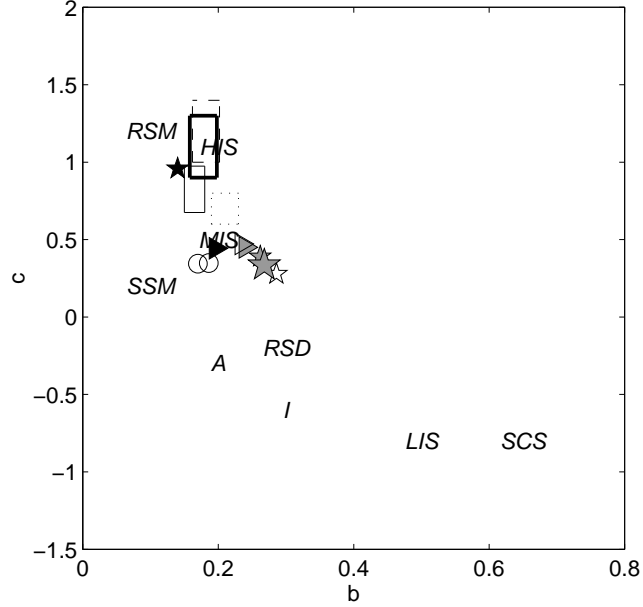


Fig. 9.— The double Henyey-Greenstein particle angular scattering function coefficients b and c for the V-band of Mercury and the Moon, plotted in relation to the properties of single particles studied by McGuire and Hapke (1995). Rectangular areas are solutions derived in this work; the area defined by a thick solid line is the solution based on the Mallama *et al.* (2002) phase curve for Mercury (Sol. 1 in Table 1), the thin solid line box is the analog solution but with the restriction $\alpha < 145^\circ$ (Sol. 3), the dashed-line rectangle marks the solution from SVST disk-resolved image profiles of Mercury constrained by the phase curve (Sol. 7), while the dotted rectangle is the solution of the lunar integral phase curve from observations of Rougier (1933) (Sol. 4). Pentagrams indicate the solutions determined by Helfenstein and Veverka (1987) for different lunar surface types: highlands (white), average Moon (gray), and maria (black); the large gray pentagram indicates their solution from the integral phase curve. Triangles give the corresponding lunar solutions of Veverka *et al.* (1988), while circles mark their two solutions for the integral mercurian phase curve. The acronyms for particle types are (from McGuire and Hapke 1995) smooth clear sphere (SCS), low density of internal scatterers (LIS), irregular shape (I), rough-surfaced dielectric (RSD), agglomerates (A), smooth-surfaced metal (SSM), medium density of internal scatterers (MIS), high density of internal scatterers (HIS), and rough-surfaced metal (RSM).

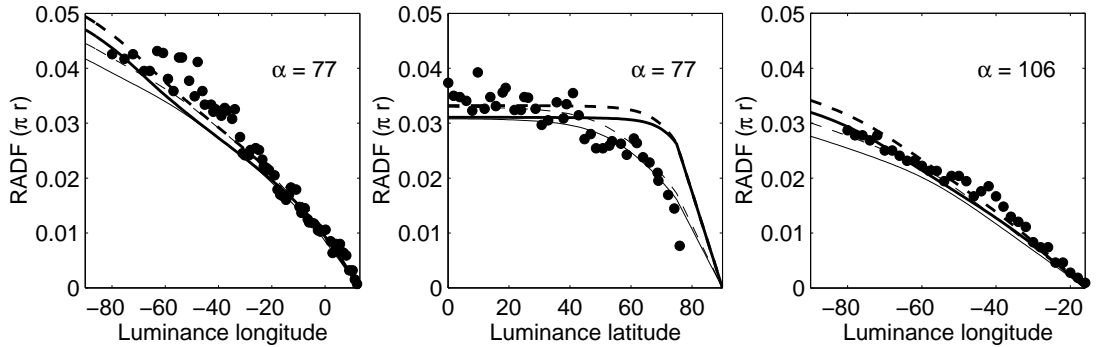


Fig. 10.— Disk-resolved scans of Mercury from Mariner 10 full-disk images (dots) compared to brightness profiles derived in this paper. The left and central panels display respectively brightness scans along the luminance equator and -50° luminance longitude (both data sets from Hapke 1984) at a phase angle of 77° , while the right panel shows a luminance equator profile (binned data, from Mallama *et al.* 2002) at a phase angle of 106° . The thick solid lines are based on the photometric parameter solution derived from Earth-based disk-resolved SVST images (Warell and Limaye 2001) with phase curve constraint (Sol. 7), while the thick dashed lines are modelled from the Mallama *et al.* (2002) integral phase curve only (Sol. 1). Narrow lines are derived with parameters equal to the respective nominal solutions, but with $\bar{\theta} = 16^\circ$. All Mariner 10 data have been decreased in brightness by 10% to fit the modelled intensity derived from the integral phase curve (Sol. 1).